



# Magnetic modulation of far- and near-field IR properties in rod-slit complementary spintronic metasurfaces

GASPAR ARMELLES,<sup>1,\*</sup> LUCA BERGAMINI,<sup>2,3</sup> ALFONSO CEBOLLADA,<sup>1</sup>  M. UJUÉ GONZÁLEZ,<sup>1</sup> RAQUEL ÁLVARO,<sup>1</sup> LORENA TORNÉ,<sup>1</sup> NEREA ZABALA,<sup>2,3</sup> AND JAVIER AIZPURUA<sup>3</sup>

<sup>1</sup>*Instituto de Micro y Nanotecnología, IMN-CNM-CSIC, Isaac Newton, 8, Tres Cantos, Madrid, 28760, Spain*

<sup>2</sup>*Department of Electricity and Electronics, FCT-ZTF, UPV-EHU, Bilbao 48080, Spain*

<sup>3</sup>*Materials Physics Center, CSIC-UPV/EHU and DIPC, San Sebastian 20018, Spain*

\**Gaspar.armelles@csic.es*

**Abstract:** Complementary metasurfaces composed of randomly-placed arrays of aligned rods or slits are fabricated out of giant magnetoresistance Ni<sub>81</sub>Fe<sub>19</sub>/Au multilayers (MLs), a material whose optical properties change under the application of an external static magnetic field. The two metasurfaces are studied from both the experimental and theoretical viewpoints. The induced magnetic modulation (MM) of both the far-field signal and the resonant near field, at the rod/slit localized surface plasmon frequency, are found to obey the Babinet's principle. Furthermore, the near-field MM is found to be higher than the far-field counterpart. At resonance, both arrays show spots with high values of the magnetic modulated intensity of the electric near field (MM hot-spots). We show that this high magnetic modulation of the near-field intensity is very promising for the future development of high sensitivity molecular sensing platforms in the Mid- and Far-IR, using Magnetic-Modulation of Surface-Enhanced Infrared Absorption (MM-SEIRA) spectroscopy

© 2020 Optical Society of America under the terms of the [OSA Open Access Publishing Agreement](#)

## 1. Introduction

Plasmonic metasurfaces constitute 2D materials capable of performing a great variety of optical functions by manipulating electromagnetic waves from the visible to the microwave spectral range. Their versatility is based on the smart arrangement of specially designed optical antenna units which constitute the building blocks of the artificial 2D material [1]. Using these platforms, wave front shaping, polarization manipulation of light, or non-linear optical conversion have already been achieved, with the further advantage of reducing the size and weight of the optical devices [2]. Moreover, metasurfaces also offer the possibility of designing the near-field response of the material, with potential applications such as sensing and optical trapping [3,4,5,6]. A further step to increase the versatility of metasurfaces is to incorporate in their design active components, i.e., materials whose optical response could be changed by applying an external stimulus [7,8]. This is the case of giant magnetoresistance multilayers (GMR MLs), which have been very recently included in the list of components for the fabrication of active metasurfaces [9,10,11]. In GMR materials, the magnetic field induced change in resistivity results in a change of the optical properties, due to the Magneto Refractive Effect (MRE) [12,13,14,15], allowing for fast and contactless modulation of the optical response of the spintronic metasurface in the Mid and Far IR. Among some of the simplest examples of plasmonic metasurfaces we note the systems composed of metallic rods or slits, as fundamental units producing electric and magnetic dipolar response, respectively. The rod electric dipole originates from collective, coherent oscillations of conduction electrons spatially confined in the rod itself (Localized Surface Plasmons, LSPs),

whereas the slit magnetic dipole is generated by extended currents occurring around the slits. At resonance, these two complementary antenna units are characterized by a very different distribution of the electric component of the near field, with maxima at the ends of the rods (for longitudinal exciting electric field) and at the central interior part of the slits (for transversal exciting electric field) [16]. Due to the different nature of both antenna units, as well as to the different spatial electromagnetic (EM) distribution of their corresponding resonances, one might expect that they are affected in a different way by the magneto-refractive effect, producing, for instance, magnetic modulation of the optical response with different intensities, spatial distribution or spectral dependence.

In this work we compare the magnetic modulation (MM) of both the near- and far-field electromagnetic properties of pre-designed disordered arrays of aligned rods and slits fabricated out of GMR  $\text{Ni}_{81}\text{Fe}_{19}/\text{Au}$  multilayers. Both rods and slits have the same sizes and, according to Babinet's principle, they are complementary antenna units whose resonance has a strong electric dipolar (rods) or magnetic dipolar (slits) character [17,18,19,20,21]. We first explored the MM of the far-field response of the two metasurfaces, by investigating the MM of the rods in transmission and the MM of the slits in reflection. Then, we studied the MM of the electromagnetic near field produced by the rods and slits at the plasmon resonance. Since the plasmon resonance is characterized by an electric and magnetic dipolar character for the rods and slits, respectively, the electric field of the rods was compared with the magnetic field of the slits. Finally, we extended our study by focusing on the potential of these metasurfaces for sensing. Similarly to the well-known plasmonic hot-spots, where the electric field is highly enhanced when the plasmon resonance is excited, in this work we found regions close to the antenna units where the MM of the electric field intensity is also enhanced (MM hot-spots). This behaviour can be exploited to carry out molecular sensing based on magnetic modulation (MM-SEIRA), with perspectives of improved performance with respect to standard SEIRA at specific locations close to the antenna units.

## 2. Results and discussion

Randomly placed aligned rods and slits arrays (the orientation of the rods/slits is the same for all of them but their position within the array is random) were fabricated on 50 nm thick  $\text{Ni}_{81}\text{Fe}_{19}/\text{Au}$  multilayers grown at 150°C on  $\text{CaF}_2$  (111) single crystalline substrates. First, a 2 nm thick Ti buffer layer was deposited by electron beam evaporation. Then, a 2.4 nm thick Au layer was sputtered followed by a 2.8 nm thick  $\text{Ni}_{81}\text{Fe}_{19}$  layer also deposited by sputtering. This bi-layer deposition was repeated 8 times, after which a final 5 nm Au thick layer was deposited on top of the multilayer to protect it against oxidation. The multilayer exhibits 4% GMR and a saturation magnetic field of 50 Oe [22,23]. Sketches of these elements are shown in Figs. 1(a) and 1(b). The random arrangement has been chosen to avoid diffraction effects linked to ordered structures and, in the case of the slits, minimize the excitation of propagating plasmons, leaving their optical response reduced to a featureless contribution from the inter-slit continuous region and the slit localized resonance. Both types of elements are fabricated by electron beam lithography and etching of the continuous  $\text{Ni}_{81}\text{Fe}_{19}/\text{Au}$  multilayer film in an area of  $100 \times 100 \mu\text{m}^2$ . The random pattern was obtained with an algorithm that generated random positions for each element (rod or slit) and then excluded those positions that were closer than a certain predefined distance in order to reduce interaction effects.

Two couples of arrays were fabricated, with rods and slits 300 nm wide, and with 2 and 3  $\mu\text{m}$  in length. Identical random patterns were used for each complementary couple to make a direct comparison straightforward. The resulting areal concentration of rods and slits is 2.1% for all the structures. SEM images of the obtained rods and slits complementary metasurfaces are shown in Figs. 1(c) and 1(d) for 2  $\mu\text{m}$  long and in Figs. 1(e) and 1(f) for 3  $\mu\text{m}$  long antenna units

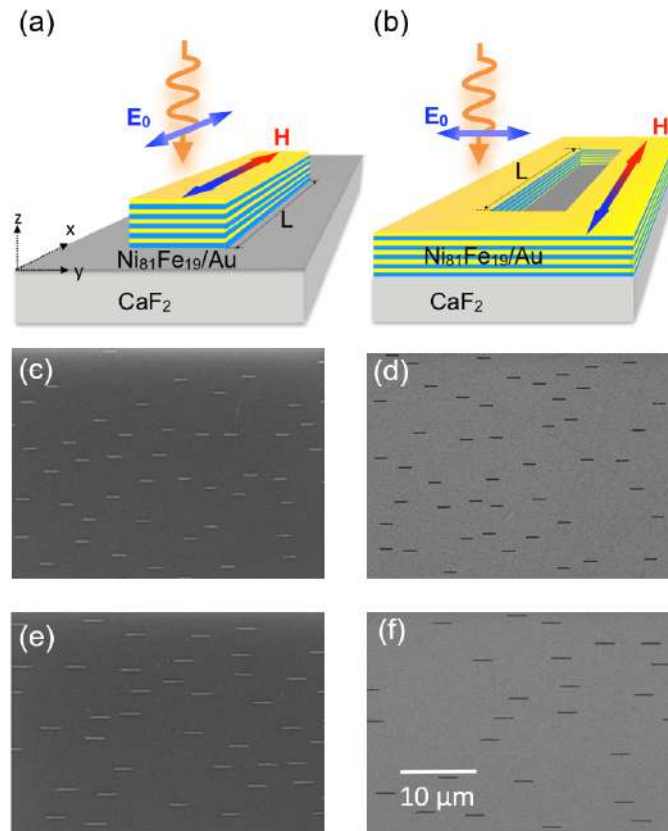


**Fig. 1.** Sketch of GMR multilayer (a) nanorods and (b) slits on  $\text{CaF}_2$  substrate. Incident light polarization (i.e., incident electric field  $E_0$ ) is indicated by the blue double arrow. The coloured double arrow marks the direction of the applied external magnetic field (H). (c), (d): SEM images of the fabricated random arrays of  $2\ \mu\text{m}$  rods (c) and slits (d). (e), (f): SEM images of the fabricated random arrays of  $3\ \mu\text{m}$  rods (e) and slits (f).

### 2.1. Magnetic modulation of the transmission/reflection of Babinet-complementary rods/slits metasurfaces

When dealing with structures that are complementary according to Babinet's principle, it has been established that several magnitudes exchange their roles, such as the optical transmission and reflectivity, electric and magnetic fields, and polarization directions [18,24]. As such, both nanorods transmission and slits reflectivity spectra were obtained using an IR microscope (Hyperion) coupled to a FTIR spectrometer (Bruker Vertex 70). The nanorods transmission spectra (T) were normalized to the transmission of the  $\text{CaF}_2$  substrate, whereas the slits reflectivity spectra (R) were normalized to the reflectivity of the continuous multilayer. In Fig. 2(a) we present the transmission spectra of the rods for light polarized along their long axis (solid red ( $2\ \mu\text{m}$ ) and blue ( $3\ \mu\text{m}$ ) lines). As observed, both spectra show a dip corresponding to the excitation of the electric dipolar LSP resonance of the rods [6]. The position of the dip depends on the rod length, shifting to lower energies as the length increases. Figure 2(a) also includes the reflectivity spectra of the slits (dashed red and blue lines for  $2\ \mu\text{m}$  and  $3\ \mu\text{m}$ , respectively), but now with the light polarized perpendicular to the long axis of the slit. In this second case, the observed dips in the reflectivity correspond to the excitation of the magnetic dipolar LSP

resonance of the slits, whose position also depends on the length of the resonant antenna unit [16]. This similarity between rods transmission and slits reflectivity spectra corroborates the optical complementarity of the fabricated structures. In contrast, the transmission spectra of the rods and the reflectivity spectra of the slits for light polarized perpendicular to the rods and parallel to the slits, respectively, are featureless due to the absence of resonant excitations for these polarizations in the considered spectral range [7,8]. In Fig. 2(b) we present the simulated rods transmission and slits reflectivity spectra. These simulations were performed with the use of COMSOL Multiphysics software [25], considering a finite portion of the metasurfaces where a bunch of antenna units are placed to reproduce the rod/slit surface concentration (see Appendix for details). As it can be observed, the agreement between theory and experiments is good, with narrower and more intense dips obtained theoretically.

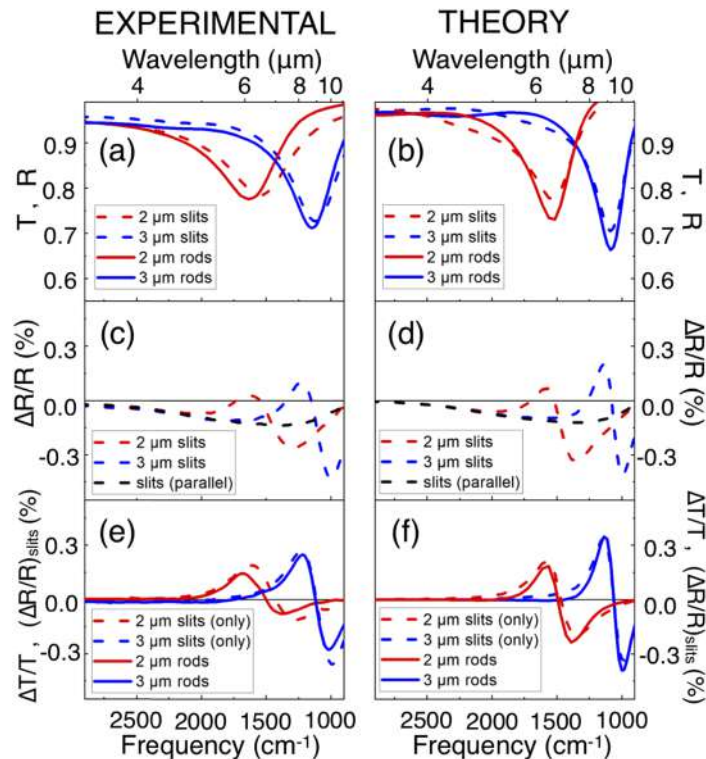


**Fig. 2.** (a), (b): Continuous lines: Experimental (a) and simulated (b) transmission spectra normalized to the  $\text{CaF}_2$  substrate for light polarized parallel to the rod long axis of a random array of 2  $\mu\text{m}$  (red line) and 3  $\mu\text{m}$  (blue line) long rods. Dashed lines: Experimental (a) and simulated (b) reflectivity spectra normalized to the continuous layer for light polarized perpendicular to the slit long axis of a random array of 2  $\mu\text{m}$  (dotted red line) and 3  $\mu\text{m}$  (dotted blue line) long slits. (c), (d): Experimental (c) and simulated (d) modulated reflectivity spectra of a random array of slits for light polarized parallel to the slit long axis (black dotted line) and perpendicular to the slit long axis (dotted red line for 2  $\mu\text{m}$  slits, dotted blue line for 3  $\mu\text{m}$  slits). (e), (f): Continuous lines: Experimental (e) and simulated (f) modulated transmission spectra of a random array of rods for light polarized parallel to the rod long axis (red line for 2  $\mu\text{m}$  rods, blue line for 3  $\mu\text{m}$  rods). Dashed lines: Experimental (e) and simulated (f) slit contribution to the modulated reflectivity of a random array of slits for light polarized perpendicular to the slit long axis (dotted red line for 2  $\mu\text{m}$  slits, dotted blue line for 3  $\mu\text{m}$  slits) [the contribution of the continuous film has been removed].

The spintronic nature of the  $\text{Ni}_{81}\text{Fe}_{19}/\text{Au}$  multilayer, with a noticeable change of electrical resistivity in the presence of moderate magnetic fields [22], leads to a change in its optical constants (Magneto Refractive Effect). Therefore, it is possible to magnetically modulate the optical response of these systems using moderate external magnetic fields (i.e., a few tens of Oe). In Fig. 2 we also present experimental (left panels, (c) and (e)) and theoretical (right panels, (d) and (f)) spectra of the normalized magnetic field induced change of the transmission and reflectivity of the rods and slits arrays, respectively. The experimental spectra were obtained by applying a magnetic field in the plane of the sample (see sketches in Figs. 1(a) and 1(b)), high enough to saturate the multilayer ( $H = H_{\text{sat}}$ ), and therefore reach the low electrical resistivity state of the ML. In this state all the magnetic moments of the ferromagnetic layers point in the same direction (from now on denoted as parallel or P state) [9,10,23]. Spectra were also recorded at zero magnetic field ( $H = 0$ ). At zero field the magnetic moments of the adjacent ferromagnetic layers are oriented in opposite direction, antiparallel or AP state, corresponding to a high electrical resistivity configuration [9,10,23]. Following this nomenclature, the plotted magnetic modulation of the reflectivity and transmission spectra correspond to  $\Delta R/R = (R_P - R_{AP})/R_{AP}$  and  $\Delta T/T = (T_P - T_{AP})/T_{AP}$ , respectively. On the other hand, the theoretical calculations were obtained using the two different optical constants of the  $\text{Ni}_{81}\text{Fe}_{19}/\text{Au}$  multilayer characterizing the large electrical resistivity, AP state (with no external magnetic field,  $H = 0$ ) and the low electrical resistivity, P state (with external magnetic field  $H = H_{\text{sat}}$ ), which were retrieved from experimental measurements.

While in the rods system the measured magnetic modulation is due exclusively to the antenna units, in the slits system the contribution from the continuous part of the film in addition to that from the slits is also present. This can be clearly seen in Fig. 2(c) (experimental data) and Fig. 2(d) (numerical data), where the normalized magnetic field induced changes of the reflectivity are shown for light polarized parallel and perpendicular to the slit axis. If the light is polarized parallel to the slits (dashed black line), the antenna magnetic dipolar resonance is not excited and the spectra for both slits arrays consist of a broad negative featureless band originated from the modulation of the multilayer film. On the other hand, when the light is polarized perpendicular to the slits (dashed red (2  $\mu\text{m}$ ) and blue (3  $\mu\text{m}$ ) lines), the magnetic dipolar resonance of the antenna units is excited and superimposed to the signal of the continuous part of the multilayer film, leading to an additional structure in the spectral range of the antenna resonance for both slits arrays. In principle, the contribution of the continuous part of the multilayer to the modulation of the reflectivity should be the same for both polarizations:  $\Delta R(\text{ML})_{\text{pol} //} = \Delta R(\text{ML})_{\text{pol} \perp}$ . Therefore, the contribution to the modulated reflectivity strictly due to the slits is  $(\Delta R/R)_{\text{slits}} = (\Delta R_{\text{pol} \perp} - \Delta R_{\text{pol} //})/R_{\text{pol} \perp}$ . The obtained spectra are presented in Fig. 2(e) (experimental data) and Fig. 2(f) (theory) for 2  $\mu\text{m}$  (dashed red) and 3  $\mu\text{m}$  (dashed blue) slits. As it can be observed, both experimental and calculated spectra are very similar, showing a derivative-like line shape consistent with the magnetic modulation of the slit resonance. Going now to the morphologically complementary system, in Figs. 2(e) and 2(f) we have also included the experimental and calculated normalized magnetic field induced changes of the transmission of the two rods arrays for light polarized along the rod axis (solid red/blue lines for 2  $\mu\text{m}$ /3  $\mu\text{m}$  rods). No magnetic modulation was observed for light polarized perpendicular to the rod axis since no rod resonance was excited (in this spectral range) and there is no multilayer film to contribute with a background modulation signal (the antennas do not produce a detectable signal by themselves). As it can be observed, the magnetic modulation spectra of both types of antennas (rods and slits) show very similar intensity and spectral shape in the complementary magnitudes of  $\Delta T/T$  and  $(\Delta R/R)_{\text{slits}}$  for both antenna unit lengths.

These results point out that the magnetic modulation of the optical response of plasmonic GMR metasurfaces which are complementary in terms of Babinet's principle shows the same

exchange relationship as the pure R and T signal, thus a similar pure and magnetic modulated far-field behaviour.

## 2.2. Near-field magnetic modulation of GMR Babinet-complementary metasurfaces

So far, we have compared, both numerically and experimentally, the magnetic modulation of the far-field response in the rods and slits arrays. As explained above, this modulation is due to the change of refractive index of the spintronic material, which constitutes the rod in one case and surrounds the slit in the other one. The very similar spectral shape of the modulated reflectivity and transmission suggests that, despite the different character of the rods/slits and of their corresponding excited dipoles, the magnetic modulation produces similar changes in the position and lifetime of these two types of LSP resonances. Since magnetic modulation effects can be very different in the far- and near-field [7], a thorough investigation of these effects in the near field is needed at this point to obtain a further insight into these aspects. The study of the magnetic modulation of the near field is specially intended to perform MM based molecular sensing with these metasurfaces.

In Fig. 3 we present a map of the spatial distribution of the normalized modulus of the electric field (Fig. 3(a)) or magnetic field (Fig. 3(b)), at a plane located 10 nm above the 2  $\mu\text{m}$  long rods or slits top surface, calculated at resonance, for the central rod (a) or slit (b) of the considered cell shown in the insets. The normalization is performed with respect to the incident electric ( $E_0$ ) or magnetic ( $H_0$ ) field, and the incident light is polarized parallel or perpendicular to the long axis of the rods or slits, respectively. As it can be observed, the two maps show very similar field distributions, typical of an electric dipole (rod) or magnetic dipole (slit), with high values of the electric or magnetic field occurring at the ends of the rods or slits, respectively. In these regions the main component of the field originates from the electric and magnetic dipole, respectively. To clearly identify this dipole contribution, we present similar maps, but for the normalized modulus of the z-component of the electric field ( $E_{AP,z}$ , Fig. 3(c)) and magnetic field ( $H_{AP,z}$ , Fig. 3(d)) for the rods and slits metasurface, respectively. Unlike the in-plane component which is the vectorial sum of the incident and the rod/slit-produced field, the z component is only due to the rod or slit dipoles ( $\mu$ ), being its intensity proportional to the intensity of the dipole. On the other hand, the dipole's intensity should be different for the P and AP states of the multilayer; therefore, in the same figure, maps of the magnetic modulation of the z component of the electric field  $\frac{|E_{P,z} - E_{AP,z}|}{|E_0|}$  (rods, Fig. 3(e)) and magnetic field  $\frac{|H_{P,z} - H_{AP,z}|}{|H_0|}$  (slits, Fig. 3(f)), induced by the change in the resistivity of the multilayer with the external magnetic field are also presented. Once again, the distribution pattern is very similar for rods and slits, and it shows the same in-plane distribution than that of the sole z component. This gives rise, in the region where the intensity of the z-component is different from zero, to a constant relative variation of the z component of the field of around 0.01 (1%) for both rods arrays ( $\frac{|E_{P,z} - E_{AP,z}|}{|E_{AP,z}|}$ ) and slits arrays ( $\frac{|H_{P,z} - H_{AP,z}|}{|H_{AP,z}|}$ ). This magnitude corresponds to the relative MM of the electric (rod) and magnetic (slit) dipoles,  $(\frac{|\Delta\mu|}{|\mu_{AP}|})$ ;  $\Delta\mu = \mu_P - \mu_{AP}$ , and determines the strength of the near-field MM properties resulting in MM intensities almost 5 times higher than the far-field ones ( $\Delta T/T$  and  $(\Delta R/R)_{\text{slits}}$  for rods and slits, respectively), which is of the order of 0.002 (0.2%).

This analysis clearly demonstrates that the near-field properties follow the same Babinet's rules found for the far-field response. Indeed, the magnetic modulated electric and magnetic near field, for rods and slits, respectively, show similar strength and spatial distribution, in accordance with the exchange rules of complementary metasurfaces. Moreover, the intensity of MM of the near field is much larger than that of the far-field properties.

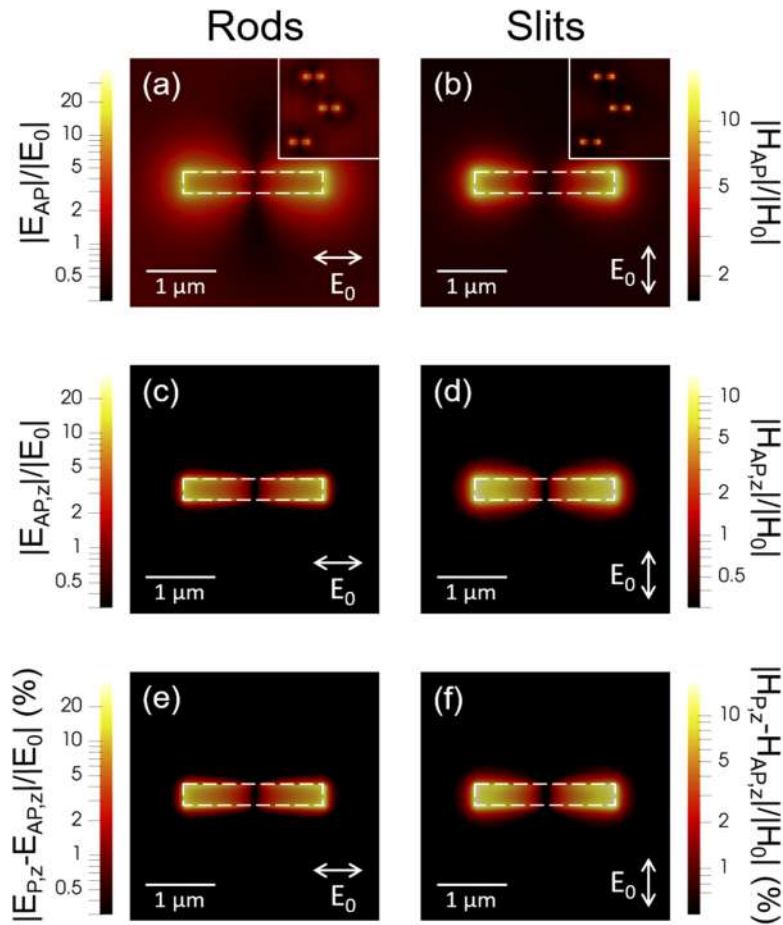


**Fig. 3.** (a): In-plane (xy) map of the normalized electric field 10 nm above the rods (length 2  $\mu\text{m}$ ), at resonance, around the central rod of the calculation cell shown in the inset. (b): In-plane (xy) map of the normalized magnetic field 10 nm above the slits (length 2  $\mu\text{m}$ ), at resonance, around the central slit of the calculation cell shown in the inset. The insets show the same map for the entire simulated cell. The colorbars hold for both the principal map and the respective inset. (c): In-plane (xy) map of the normalized z component of the electric field 10 nm above the rods (length 2  $\mu\text{m}$ ), at resonance, around the central rod of the calculation cell. (d): In-plane (xy) map of the normalized z component of the magnetic field 10 nm above the slits (length 2  $\mu\text{m}$ ), at resonance, around the central slit of the calculation cell. (e): In-plane (xy) map of the modulus of the magnetic modulation of the z-component of the electric field 10 nm above the rods (length 2  $\mu\text{m}$ ), at resonance, around the central rod of the calculation cell. (f): In-plane (xy) map of the modulus of the magnetic modulation of the z component of the magnetic field 10 nm above the slits (length 2  $\mu\text{m}$ ), at resonance, around the central slit of the calculation cell. In all maps the white dashed line marks off the rod or slit boundaries and the double white arrow represents the oscillation of the incident electric field. All maps refer to the resonant frequency of  $\omega = 1515 \text{ cm}^{-1}$  (namely, a resonant wavelength of  $\lambda = 6.6 \mu\text{m}$ ).

### 2.3. Magnetic modulated GMR metasurfaces for SEIRA applications

Finally, we explore the potential of the magnetic modulation of active metasurfaces for practical applications, given that both rods and slits arrays are widely used as platforms for Surface-Enhanced InfraRed Absorption (SEIRA) spectroscopy to detect molecular vibrations [26,27,28,29]. In SEIRA platforms the sensing magnitude is the change in the optical response due to the deposition/absorption of a layer of molecules which have some particular vibration bands. The modification of the optical response occurs at two different levels; one level is not linked to the molecular vibration but to the change of the local dielectric environment close to the rod or slit due to the deposition/absorption of the molecule. This gives rise to a frequency shift of the antenna resonance band. The other one is connected to the molecular vibration itself and appears as a very sharp feature, at the frequency of the molecular vibration, superimposed to the resonance band of the antenna unit. The spectral lineshape and intensity of this feature depends on the difference between the frequency of the molecular vibration and that of the antenna unit resonance. This specific modification of the optical response (i.e., without taking into account the effect of the change of the local dielectric environment) can be modelled as [29,30]:

$$M_{P,AP}^m(\omega) = M_{P,AP}(\omega)\{1 - f_{P,AP}(\omega)\}, \quad (1)$$

where  $M_{P,AP}^m(\omega)$  and  $M_{P,AP}(\omega)$  stand for the transmission/reflection of the rods/slits array at frequency  $\omega$  with and without the molecular vibration (i.e., base line response) for the two resistivities states, respectively, and  $f_{P,AP}(\omega)$  accounts for the absorption of the molecular vibration and leads to a Fano-like lineshape:

$$f_{P,AP}(\omega) = I_{P,AP}(\omega = \omega_{vibr}) \frac{A}{1 + q^2} \left\{ \frac{(\hat{\omega} + q)^2}{\hat{\omega}^2 + 1} - 1 \right\}. \quad (2)$$

Here  $\hat{\omega} = \frac{\omega - \omega_{vibr}}{\Gamma}$ , with  $\Gamma$  and  $\omega_{vibr}$  being the vibrational linewidth and frequency of the molecular vibration, respectively;  $q$  is the Fano parameter which depends on the difference between the frequency of the vibration and that of the antenna resonance. The parameter  $A$  determines the intrinsic strength of the vibration signal and  $I_{P,AP}$  is the intensity of the electric field of the antenna resonance at the position of the vibrating molecular bonds at the frequency of the vibration. Therefore, we can adapt this phenomenological approach to describe the effect that the light absorption of a molecule may have on the magnetic modulated signal by considering only the modification of the intensity induced by the magnetic field. In the specific case of our spintronic metasurfaces, this intensity depends on the resistivity state of the antenna units, P or AP, therefore leading to a magnetic modulated signal that can be written as (see [appendix](#)):

$$\frac{M_P^m - M_{AP}^m}{M_{AP}^m} \approx \frac{M_P - M_{AP}}{M_{AP}} - \frac{I_P - I_{AP}}{I_{AP}} \frac{f_{AP}}{(1 - f_{AP})}, \quad (3)$$

where  $M_{P,AP}^m(\omega)$  and  $M_{P,AP}(\omega)$  stand for the transmission/reflection of the rods/slits arrays for the two resistivity states of the ML, with and without the vibration, respectively. Indeed, if the electric field intensity of the antenna depends on its resistivity state, namely  $I_P \neq I_{AP}$ , the magnetic modulation spectrum should have a specific vibration feature.

With this in mind, in Figs. 4(a) and 4(b) we first present the spatial distribution of the magnetic modulation of the intensity of the electric field,  $\frac{\Delta I}{I} = \frac{I_P - I_{AP}}{I_{AP}}$ , for the same rods and slits of Fig. 3, calculated at a plane located at the middle height of the antenna units and for a frequency of  $1538 \text{ cm}^{-1}$ . Clearly the modulation of the intensity of the electric field depends both on the in-plane location and on the antenna unit type. For the rod, magnetic modulation hot-spots (MM hot-spots) are found around the ends, whereas the slit shows a fair homogeneous modulation in its interior (no feasible sensing can be considered for the middle height region around the

slit, since that would mean placing a molecule inside the multilayer). Moreover, these two high modulation regions are spatially located at plasmonic hot-spots (especially in the rods case) or at least in regions with large electric fields (for the slits case), and therefore can be considered as optimum places to locate molecules to be sensed, not only using standard SEIRA protocols, but in an implementation of SEIRA based on the modulation of the absorption produced by the magnetic field (MM-SEIRA)

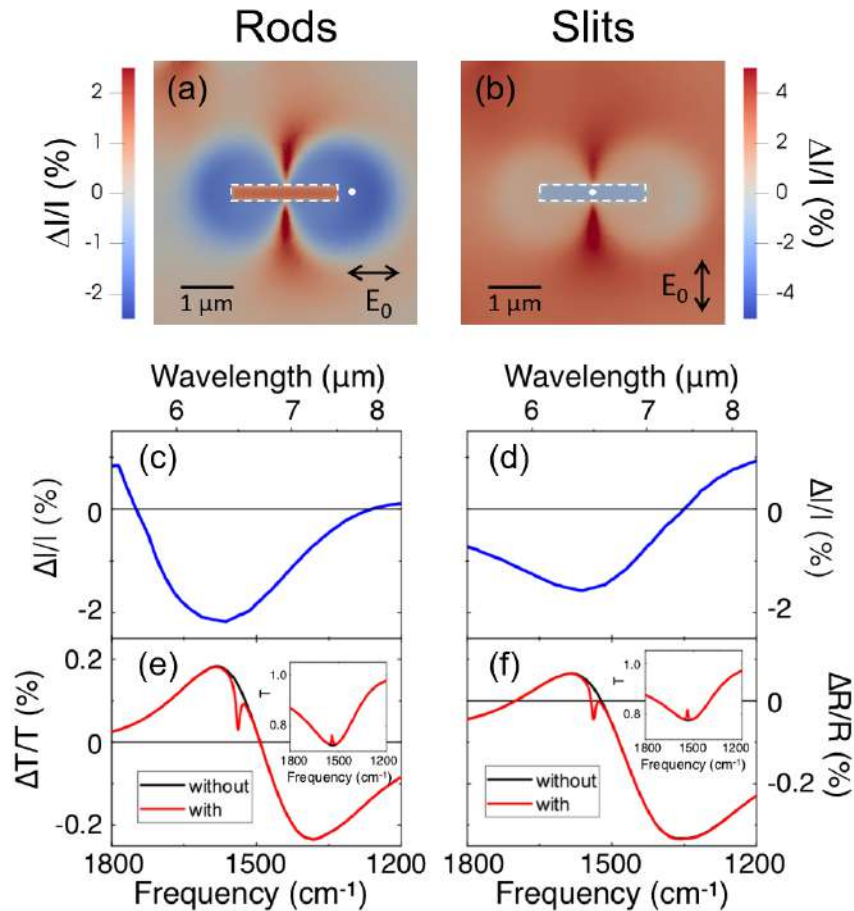


**Fig. 4.** (a), (b): In-plane ( $xy$ ) maps of the magnetic modulation of the electric field intensity,  $\Delta I/I = (I_P - I_{AP})/I_{AP}$ , at the middle height of the antenna unit, at resonance, around the central  $2 \mu\text{m}$  long rod (a) or slit (b) of the calculation cell. The white dashed line marks the rod or slit boundaries and the double white arrow represents the oscillation of the incident electric field. The two maps refer to the resonant frequency of  $\omega = 1515 \text{ cm}^{-1}$  (namely, a resonant wavelength of  $\lambda = 6.6 \mu\text{m}$ ). (c), (d): Spectral dependence of the magnetic modulation of the electric field intensity calculated at the white points in (a) and (b) for the rods (c) and slits array (d), respectively. (e), (f): Spectra of the magnetic modulation signal without a molecular vibration (black lines) and with a molecular vibration (red lines) for rods (e) and slits (f) metasurfaces, respectively. The frequency of the considered molecular vibration is  $1538 \text{ cm}^{-1}$ . The inset shows the same spectra but for direct transmission (rods) or reflection (slits).

Significantly, the modulation of the electric field intensity depends, not only on the location, but also on the frequency. In Figs. 4(c) and 4(d) we present the spectral dependence of the

modulation of the intensity of the electric field for rods and slits, calculated at two points inside the magnetic modulation hot-spots, indicated in the Figs. 4(a) and 4(b) as two white points. As it can be seen, the modulation spectral dependence is different for rods and slits, with maximum relative modulation values of the intensity of  $-0.02$  ( $-2\%$ ) for rods and  $-0.015$  ( $-1.5\%$ ) for slits at  $1538\text{ cm}^{-1}$ .

Finally, we studied the effect of a fictitious molecule with an absorption peak at  $1538\text{ cm}^{-1}$  and placed inside the MM hot-spot at the point highlighted by a white dot in Figs. 4(a) and 4(b). This effect on the magnetic modulated transmission/reflection spectra for rods and slits, is shown in Figs. 4(e) and 4(f), where we present those spectra with and without this molecular vibration (transmission/reflection spectra with and without vibration are also shown in the insets). The transmission/reflection spectra without the molecular vibration correspond to the calculated ones presented in Fig. 2(b) for the AP state, whereas those with the molecular vibration are obtained using Eq. (1), with  $M_{\text{AP}}(\omega)$  being the AP spectra without the molecular vibration and  $q=0$  (indeed the frequency of the vibration is close to the resonance frequency of the rods/slits, therefore  $q\approx 0$ ).  $I_{\text{AP}}(\omega_{\text{vibr}})$  is the COMSOL calculated intensity and the value of the parameter A has been adjusted so that the SEIRA intensity of the AP state (i.e., the intensity of the relative change of the transmission/reflection due to the molecular vibration) is  $5\%$  for both rods and slits metasurfaces. The magnetic modulation spectra (i.e., the relative change of the transmission/reflection between the two magnetic states) are obtained by calculating the spectra of the P state using also Eq. (1) but for the P state, and setting  $q$  and  $A$  to the same values of the AP spectra. Indeed, the parameter  $A$  is related to the intrinsic strength of the vibration signal and does not depend on the magnetic states of the multilayer. The Fano parameter,  $q$ , depends on the difference between the vibrational frequency and the resonance frequency, whose magnetic field dependence is very small. As it can be observed, the modulated spectra with and without the molecular vibration are different, with a sharp and intense feature at the frequency of the molecular vibration when the vibration is present. Moreover, the MM-SEIRA intensity, which is the relative change in the magnetic modulated signal due to the molecular vibration, amounts to  $77\%$  for the rods and  $240\%$  for the slits, whereas the SEIRA intensity is  $5\%$ . All these results strongly suggest that the magnetically modulated signal could be much more sensitive to detect molecular vibrations than the pure optical response, and highlight the importance of an adequate tuning to the molecular vibration frequency of the magnetic modulation spectral response of the antenna units, as well as of the spatial location of the molecules. In particular, both the enhancement of the electromagnetic field intensity at the position of the molecules, common to all SEIRA platforms, and the change of the near-field intensity at the position of the molecules induced by the external magnetic field should be taken into account (as suggested by Eq. (3)).

### 3. Conclusions

We have studied the magnetic modulation of the far- and near-field optical response of Babinet complementary plasmonic metasurfaces composed of rods and slits made out of GMR MLs. We observe an exchange relationship between the magnetic modulation of their far-field signal (namely,  $\Delta T/T$  and  $(\Delta R/R)_{\text{slits}}$ ) similar to the one characterizing the pure optical response (i.e.,  $T$  and  $R$ ). This exchange relationship is found to hold also in the near field, where a close analysis reveals similar strengths and spatial distributions between the module, the  $z$ -component module and the  $z$ -component MM module of the electric and the magnetic field for resonant rods and slits, respectively. Besides, the magnitude of the MM near-field properties turns out to be much higher than that of the far-field ones. For both metasurfaces, we have also identified regions where the magnetic modulation of the electric field is enhanced (MM hot-spots). The spatial distribution, the absolute value and the frequency dependence of this magnetic modulated intensity of the electric field strongly varies between the two metasurfaces. Indeed, for the rods arrays the highest values are found close to the ends of the rods, whereas for the slits the centre exhibits

the highest modulation (at resonance). We demonstrated that, within a SEIRA framework, the magnetic modulation of the signal is much more sensitive than the detection based on direct optical absorption of molecular vibrations.

Finally, these results highlight the relevance of exploring, in addition to the far-field properties, near-field ones, which may have great impact on practical applications like sensing, where local properties are most significant. On the other hand, these spintronic MM-SEIRA metasurfaces appear to be excellent candidates to improve the detection capability of traditional SEIRA platforms and develop high sensitivity Mid- and Far-IR sensors, as suggested by our study.

## Appendix

### *Effects of molecular vibrations on the magnetic modulated spectra*

The specific modification that the sharp absorption band of a molecular vibration produces on the optical transmission of an array of GMR antennas can be simulated for the two resistivity states, P and AP, as [29,30] :

$$T_{P,AP}^m = T_{P,AP} \{1 - f_{P,AP}(\omega)\}, \quad (4)$$

where

$$f_{P,AP}(\omega) = I_{P,AP}(\omega = \omega_{vibr}) \hat{f}(\omega), \quad (5)$$

and

$$\hat{f}(\omega) = \frac{A}{1 + q^2} \left\{ \frac{(\hat{\omega} + q)^2}{\hat{\omega}^2 + 1} - 1 \right\}. \quad (6)$$

$\hat{f}(\omega)$  is a function which takes into account the bonds absorption and their interaction with the antenna resonance. It has a Fano-like lineshape, being  $q$  the Fano parameter;  $\hat{\omega} = \frac{\omega - \omega_{vibr}}{\Gamma}$ , with  $\Gamma$  and  $\omega_{vibr}$  the vibrational linewidth and frequency of the molecular band, respectively.  $A$  is a parameter related to the number of molecular bonds and the intrinsic absorption strength of the bonds.  $I_{P,AP}(\omega = \omega_{vibr})$  is the intensity of the electric field of the antenna at the position of the bonds and at the frequency of the vibration  $\omega_{vibr}$  for the two resistivity states of the antenna, P and AP, respectively.  $T_{P,AP}$  stands for the transmission without the sharp absorption band (base line transmission).

Therefore, the effect on the magnetic modulation of the transmission can be written as:

$$\frac{\Delta T^m}{T_{AP}^m} = \frac{T_P^m - T_{AP}^m}{T_{AP}^m} = \frac{(T_P - T_{AP}) - \hat{f}(T_P I_P - T_{AP} I_{AP})}{T_{AP}(1 - I_{AP} \hat{f})} = \frac{\Delta T}{T_{AP}} - \frac{\Delta I}{I_{AP}} \frac{I_{AP} \hat{f}}{(1 - I_{AP} \hat{f})} \left(1 + \frac{\Delta T}{T_{AP}}\right), \quad (7)$$

with  $\Delta T^m = T_P^m - T_{AP}^m$ ,  $\Delta T = T_P - T_{AP}$  and  $\Delta I = I_P - I_{AP}$ . If  $\Delta T \ll T_{AP}$

$$\frac{\Delta T^m}{T_{AP}^m} \approx \frac{\Delta T}{T_{AP}} - \frac{\Delta I}{I_{AP}} \frac{I_{AP} \hat{f}}{(1 - I_{AP} \hat{f})} = \frac{\Delta T}{T_{AP}} - \frac{\Delta I}{I_{AP}} \frac{f_{AP}}{(1 - f_{AP})}. \quad (8)$$

For simplicity the dependence of  $\frac{\Delta T^m}{T_{AP}^m}$ ,  $\frac{\Delta T}{T_{AP}}$ ,  $\hat{f}$  on  $\omega$  and  $\frac{\Delta I}{I_{AP}}$ ,  $I_{AP}$  on  $\omega_{vibr}$  has been omitted.

A similar expression can be obtained for the reflectivity:

$$\frac{\Delta R^m}{R_{AP}^m} \approx \frac{\Delta R}{R_{AP}} - \frac{\Delta I}{I_{AP}} \frac{f_{AP}}{(1 - f_{AP})}, \quad (9)$$

with  $\Delta R^m = R_P^m - R_{AP}^m$  and  $\Delta R = R_P - R_{AP}$ .

As it can be observed, the modifications on the magnetic modulated spectra depend on the magnetic modulation of the near field at the position of the molecular bonds and at the frequency of the molecular vibration.

As an example, in Figs. 4(e), 4(f) and insets we present the calculated spectra for the four magnitudes (transmission, reflectivity and modulated transmission and modulated reflectivity) for molecular bonds with a vibration band at the resonance of the antenna,  $\omega_{vibr} = 1538 \text{ cm}^{-1}$  and  $q=0$ , with a vibrational line width of  $5 \text{ cm}^{-1}$ . The parameter A has been adjusted so that the relative change of the transmission/reflection produced by the introduction of the molecular vibration (SEIRA intensity) is 5% for both rods and slits metasurfaces.

On the other hand, mention also that the enhancement of the SEIRA signal with respect to the system without antennas is of the order of 3 and 7500 for the rods and slits array, respectively. In the case of the rods array, this enhancement is calculated by comparing the transmission of the system, with the molecule placed at the white point of Fig. 4(a) with the transmission of a simple  $\text{CaF}_2$  substrate with a molecule placed on its surface. Similarly, the SEIRA enhancement for the slits array is calculated by comparing the reflectivity of the system, with the molecule placed at the center of the slit (as pictured in Fig. 4(b)), with the transmission of a 55 nm tall GMR ML continuous film on top of a  $\text{CaF}_2$  substrate, with a molecule deposited on its surface

#### *Optical and magnetic-modulation characterization of the multilayer film and the substrate*

Fourier Transform infrared (FTIR) transmission and reflectivity measurements in a continuous GMR multilayer film, both with and without applied external DC magnetic field, allow for the experimental determination of the spectral dependence of the  $\text{Ni}_{81}\text{Fe}_{19}/\text{Au}$  multilayer complex refractive index and its magnetic modulation. Due to the multilayer structure the effective in-plane optical constants (xx and yy components) and the perpendicular optical constant (zz component) of the multilayer could be different. In Figs. 5(a-d) we present the effective in-plane refractive index and its magnetic modulation. At normal incidence the optical response is mainly determined by the in-plane optical constants and the difference between the in-plane and perpendicular optical constants, which are expected to be small [31], can be neglected. These experimental values, displayed in Figs. 5(a)–5(d) are then available as input parameters for the calculations performed in the present work.

The refractive index of  $\text{CaF}_2$ , used as a substrate, is displayed in Fig. 5(e) and Fig. 5(f).

#### *Electromagnetic calculations of the IR transmission/reflectivity spectra*

We performed full electro-dynamical calculations of the optical reflectivity of the investigated GMR-plasmonic platforms, shown in Figs. 2, 3 and 4, by adopting the Finite-Element-Method (FEM) implemented in the COMSOL Mutiphysics software [25].

According to the experimental setup, we modelled the random rod array systems as a compound of parallelly-oriented randomly-placed 55 nm tall antennas placed on a  $\text{CaF}_2$  substrate and embedded in air (see sketch in Fig. 6(a)). On the other hand, we modelled the random slit array systems as a 55 nm thick film of the  $\text{Ni}_{81}\text{Fe}_{19}/\text{Au}$  multilayer (ML) on a  $\text{CaF}_2$  substrate surrounded by air. An isolated compound of parallelly-oriented randomly-placed slits (see sketch in Fig. 6(b)) was drilled inside the film. Following the experimental characterization, we chose the rods/slits to be  $0.3 \mu\text{m}$  in width (W) and with a length (L) of either  $2 \mu\text{m}$  or  $3 \mu\text{m}$ . With the aim of finely tuning the structure to the real samples, both the rod and the slit in-plane ends were rounded with a radius of about 25 nm.

For the simulation of isolated random rods/slits compounds, we considered 3 rods/slits as placed inside a reference area. The size of the reference area was fixed of either  $9 \mu\text{m} \times 9 \mu\text{m}$  or  $11 \mu\text{m} \times 11 \mu\text{m}$ , for the  $2 \mu\text{m}$  and  $3 \mu\text{m}$  long rods/slits, respectively, to reproduce the experimental concentration in area of 2.1%. The simulation box size was set to  $(9 + 12/2+\lambda) \mu\text{m} \times (9 + 12/2+\lambda) \mu\text{m} \times 10 \mu\text{m}$  (length x width x height), where  $\lambda$  is the simulated wavelength. The arrangement for  $2 \mu\text{m}$  long rods/slits is represented in Figs. 6(a) and 6(b) (similar arrangements are used for the  $3 \mu\text{m}$  long rods/slits). In all cases the simulation box was surrounded by a Perfect Matching Layer [25] (PML) to mimic an infinite space.

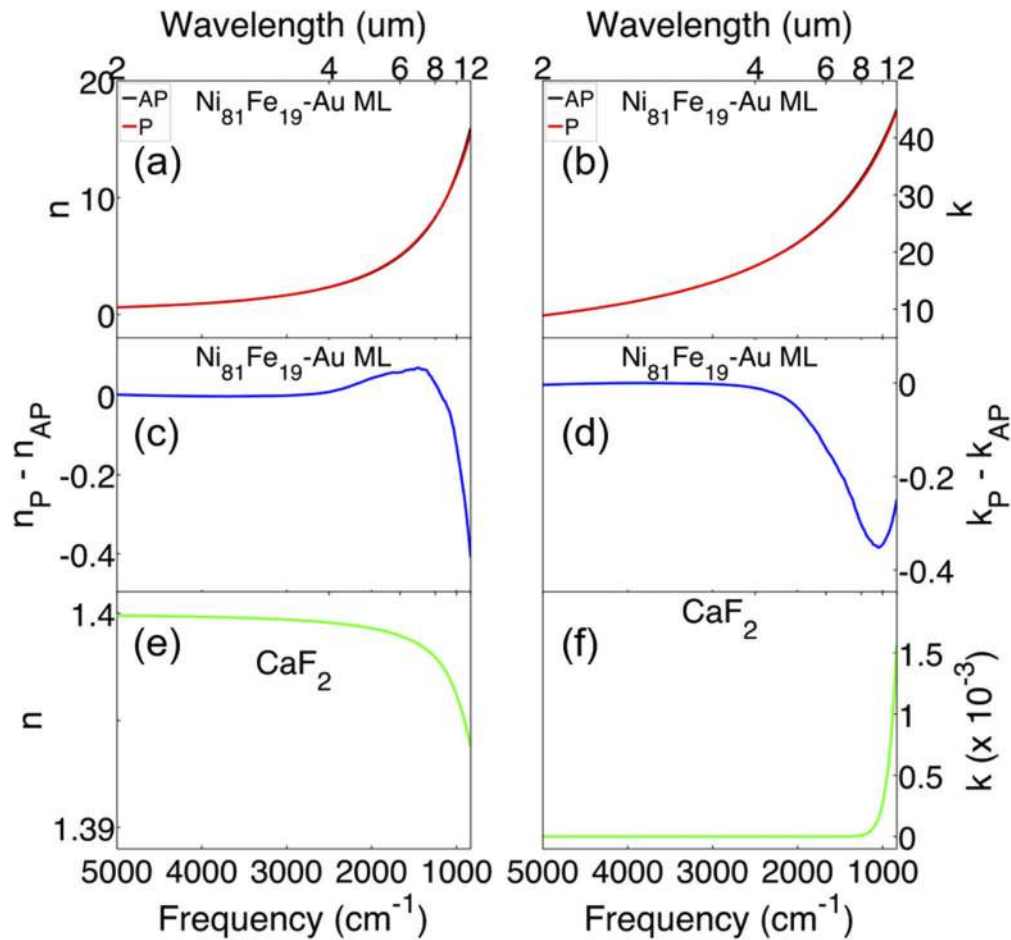


**Fig. 5.** (a) Real and (b) imaginary part of the experimental in plane refractive index of the  $\text{Ni}_{81}\text{Fe}_{19}\text{-Au}$  multilayer with (red, P) and without (black, AP) applied external DC magnetic field  $H$ . Modulation induced by the application of the external DC magnetic field on the (c) real and (d) imaginary part of the experimental refractive index of the  $\text{Ni}_{81}\text{Fe}_{19}\text{/Au}$  multilayer. (e) Real and (f) imaginary part of the experimental refractive index of the  $\text{CaF}_2$ .

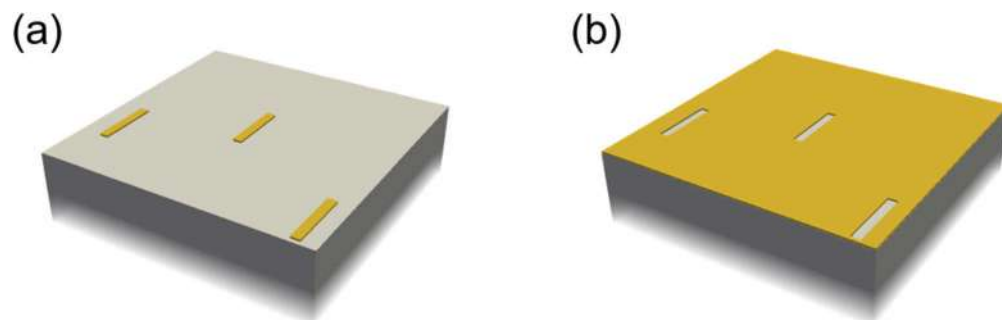


**Fig. 6.** Sketch of the simulated reference area for the random array system composed of  $2\ \mu\text{m}$  long (a) rods and (b) slits. The  $9\ \text{mm} \times 9\ \text{mm}$  reference area is represented. The orange and grey colors refer to the  $\text{Ni}_{81}\text{Fe}_{19}\text{-Au}$  multilayer and  $\text{CaF}_2$  material, respectively.

For the optical characterization, the refractive indices of both the CaF<sub>2</sub> substrate and the Ni<sub>81</sub>Fe<sub>19</sub>/Au ML material were experimentally obtained as described in the previous section of this appendix. For describing the optical properties of the Ni<sub>81</sub>Fe<sub>19</sub>/Au ML under no applied external DC magnetic field (H) we used a scalar complex permittivity  $\tilde{\epsilon}_{AP}(\omega)$  with  $\omega = 2\pi/\lambda$  being the frequency of the incident radiation. Its value is attained on the ground of the experimental data (shown in Fig. 5) via the relation:

$$\tilde{\epsilon} = \tilde{n}^2 = (n + ik)^2, \quad (10)$$

where  $\tilde{\epsilon}$  is the scalar complex permittivity,  $n$  and  $k$  the real and imaginary part, respectively, of the corresponding scalar complex refractive index  $\tilde{n}$ . To reproduce the optical behavior of the Ni<sub>81</sub>Fe<sub>19</sub>/Au ML under the application of an external DC magnetic field parallel to the CaF<sub>2</sub> surface, we use the tensorial permittivity:

$$\tilde{\tilde{\epsilon}}_P(\omega) = \begin{pmatrix} \tilde{\epsilon}_P(\omega) & 0 & 0 \\ 0 & \tilde{\epsilon}_P(\omega) & 0 \\ 0 & 0 & \tilde{\epsilon}_{AP}(\omega) \end{pmatrix}, \quad (11)$$

where  $\tilde{\epsilon}_P(\omega)$  is calculated on the basis of the experimental data (see Fig. 5).

The incident radiation was modelled as a plane-wave perpendicular to the sample surface, with the electric field aligned either along the long or the short axis of the rods/slits.

The concerned quantities are the optical transmission and the reflectivity for the rods and slits system, respectively. The simulated transmission ( $T = T_{AP}$ ) and reflectivity ( $R = R_{AP}$ ) spectra shown in this study are all obtained by endowing the rods or the slit-drilled continuous GMR film with the scalar permittivity  $\tilde{\epsilon}_{AP}(\omega)$ , respectively. The calculations were performed over the concerned wavelength window, namely between 2  $\mu\text{m}$  and 12  $\mu\text{m}$ , with a wavelength step of 200 nm. These calculations were realized by using the ‘‘Electromagnetic Waves, Frequency Domain’’ COMSOL module in combination with a ‘‘Frequency Domain Study’’, which determines the electromagnetic field in the simulation domain. By knowing the electromagnetic field on a plane area (monitor) placed 3  $\mu\text{m}$  below or above the CaF<sub>2</sub> surface, for the rods and slits compound, respectively, and integrating the time-averaged Poynting vector on it, we retrieved the total transmission and reflectivity through the formulae:

$$T^{tot} = \frac{\int_{A_T} \frac{1}{2} \text{Re} \left\{ \tilde{\tilde{E}}_T^* \times \tilde{\tilde{H}}_T \right\} \cdot \hat{n}_T dA_T}{P_0}, \quad (12)$$

$$R^{tot} = \frac{\int_{A_R} \frac{1}{2} \text{Re} \left\{ \tilde{\tilde{E}}_R^* \times \tilde{\tilde{H}}_R \right\} \cdot \hat{n}_R dA_R}{P_0}, \quad (13)$$

where  $A_T$  ( $A_R$ ) is the area of the transmission (reflectivity) plane,  $P_0$  the power of the incident radiation over the same area,  $\hat{n}_T$  ( $\hat{n}_R$ ) the transmission (reflectivity) plane-normal unitary vector,  $\tilde{\tilde{E}}_T$  ( $\tilde{\tilde{E}}_R$ ) and  $\tilde{\tilde{H}}_T$  ( $\tilde{\tilde{H}}_R$ ) the transmitted (reflected) electric and magnetic field (the sum of the slit-scattered and film-reflected electric and magnetic field namely the total electromagnetic field minus the incident one) recorded on the monitor, respectively. The distance between the monitor and the surface is a feasible distance from the simulation point of view, taking into account the impossibility of simulating a monitor at distances of the order of centimeters with a micrometer system. Indeed, the required size of the simulation box would lead to too RAM-demanding, time-consuming calculations and the combination mesh-distance to be simulated (between the sample surface and the monitor) would add significant numerical errors to the light propagation.

For both the transmission and the reflectivity monitor the size was chosen to be  $10.25 \mu\text{m} \times 10.25 \mu\text{m}$  or  $12.25 \mu\text{m} \times 12.25 \mu\text{m}$  for the  $2 \mu\text{m}$  and  $3 \mu\text{m}$  long rods/slits system, respectively. Since in the experiments the actual incident and collecting angle of the light ranges from  $0^\circ$  to  $23.58^\circ$ , different sizes of the monitor were tested in order to mimic the experimental measurements, namely we ensured that the collected light angles in the simulations reproduce those of the experiments (i.e., that the experimental reflectivity shape, not the intensity, is reproduced). Nevertheless, for a quantitative comparison, both the transmission and the reflectivity were normalized following two steps. First, we calculated the contribution of one rod/slit to the simulated transmission/reflectivity ( $T^{rod}/R^{slit}$ ), given by the formula:

$$T^{rod} = (T^{sub} - T^{tot}) * \left( \frac{A_T}{n_r * W * L} \right), \quad (14)$$

$$R^{slit} = (R^{sub} - R^{tot}) * \left( \frac{A_R}{n_s * W * L} \right), \quad (15)$$

with  $n_r = 3$  ( $n_s = 3$ ) being the number of simulated rods (slits) and  $T^{sub}$  the transmittivity obtained by the same monitor for a bare  $\text{CaF}_2$  substrate ( $R^{sub}$  the reflectivity obtained by the same monitor for a pure multilayer film without slits). Next, the renormalized transmittivity and reflectivity, which are the ones displayed in the figures, were calculated according to the equation:

$$T = T^{sub} - x_r * T^{rod}, \quad (16)$$

$$R = R^{sub} - x_s * R^{slit}, \quad (17)$$

where  $x_r$  ( $x_s$ ) is the rods (slits) areal concentration of the concerned experimental sample.

For the differential spectra (see Figs. 2, 3, and 4), we also calculated the transmittivity/reflectivity when an external DC magnetic field is applied ( $T_P/R_P$ ). The calculations were performed using the same method as previously, but bestowing the permittivity  $\tilde{\epsilon}_P(\omega)$  on the  $\text{Ni}_{81}\text{Fe}_{19}$ -Au multilayer material. Therefore, the differential transmittivity and reflectivity (or magnetic modulation of the transmittivity and reflectivity)  $\Delta T/T$  and  $\Delta R/R$  are obtained from:

$$\frac{\Delta T}{T} = \frac{T_P - T_{AP}}{T_{AP}}, \quad (18)$$

$$\frac{\Delta R}{R} = \frac{R_P - R_{AP}}{R_{AP}}. \quad (19)$$

Last, we address some notes on the used mesh during the FEM simulations. In all the simulations, the mesh was chosen such that the linear size of each tetrahedral element inside the simulation domain was smaller than  $300 \text{ nm}$  (i.e., 7 times smaller than the minimum concerned wavelength). Moreover, for both the random rods and slits system, we set up a refined mesh for the rods/slits: the face parallel to the substrate surface was triangularly meshed and then extruded along the rod/slit height by dividing it in 11 parts. In addition, we meshed the rod/slit face parallel to the substrate interface with triangular pieces with maximum linear size of  $50 \text{ nm}$  and we mapped the in-plane rod/slit edge through a polygonal curve with segments of maximum length equal to  $25 \text{ nm}$ . These mesh conditions were verified to satisfy simulation convergence.

## Funding

Ministerio de Economía y Competitividad (AMES (MAT 2014-58860-P), CSIC13-4E-1794, MIRRAS(MAT2017-84009-R), PID2019-107432GB-I00, Quantum Spin Plasmonics (FIS2015-72035-EXP)); Ekonomiaren Garapen eta Lehiakortasun Saila, Eusko Jaurlaritza (KK-2018/00001); Hezkuntza, Hizkuntza Politika Eta Kultura Saila, Eusko Jaurlaritza (No. IT-1164-19); Comunidad de Madrid (S2013/ICE- 2822 (Space-Tec), SINOXPPOS-CM (S2018/BAA-4403)).

## Acknowledgments

We acknowledge financial support from MINECO through projects AMES (MAT 2014-58860-P), Quantum Spin Plasmonics (FIS2015-72035-EXP), MIRRAS(MAT2017-84009-R), and Comunidad de Madrid through project SINOXPPOS-CM (S2018/BAA-4403). We acknowledge the service from the MiNa Laboratory at IMN and funding from MINECO under project CSIC13-4E-1794 and from CM under project S2013/ICE- 2822 (Space-Tec), both with support from EU (FEDER, FSE). L.B., N.Z., and J.A. acknowledge support from the Department of Education, Research and Universities of the Basque Government through project ref. No. IT-1164-19, the Department of Industry of the Basque Government through project KK-2018/00001, and the Spanish MICIN through project ref. No. PID2019-107432GB-I00.

## Disclosures

The authors declare no conflicts of interest.

## References

1. N. Yu and F. Capasso, "Flat optics with designer metasurfaces," *Nat. Mater.* **13**(2), 139–150 (2014).
2. A. Li, S. Singh, and D. Sievenpiper, "Metasurfaces and their applications," *Nanophotonics* **7**(6), 989–1011 (2018).
3. M. Beruete and I. Jáuregui-López, "Terahertz Sensing Based on Metasurfaces," *Adv. Opt. Mater.* **8**(3), 1900721 (2020).
4. E. Hendry, R. V. Mikhaylovskiy, L. D. Barron, M. Kadodwala, and T. J. Davis, "Chiral electromagnetic fields generated by arrays of nanoslits," *Nano Lett.* **12**(7), 3640–3644 (2012).
5. M. Schaferling, X. Yin, and H. Giessen, "Formation of chiral fields in a symmetric environment," *Opt. Express* **20**(24), 26326 (2012).
6. M. Juan, M. Righini, and R. Quidant, "Plasmon nano-optical tweezers," *Nat. Photonics* **5**(6), 349–356 (2011).
7. G. Armelles, A. Cebollada, F. García, A. García-Martín, and N. de Sousa, "Far- and Near-Field Broad-Band Magneto-Optical Functionalities Using Magnetoplasmonic Nanorods," *ACS Photonics* **3**(12), 2427–2433 (2016).
8. G. Armelles, A. Cebollada, H. Y. Feng, A. García-Martín, D. Meneses-Rodríguez, J. Zahao, and H. Giessen, "Interaction Effects Between Magnetic and Chiral Building Blocks: A New Route for Tunable Magneto-chiral Plasmonic Structures," *ACS Photonics* **2**(9), 1272–1277 (2015).
9. G. Armelles, L. Bergamini, N. Zabala, F. García, M. L. Dotor, L. Torné, R. Alvaro, A. Griol, A. Martínez, J. Aizpurua, and A. Cebollada, "Metamaterial Platforms for Spintronic Modulation of Mid-Infrared Response under Very Weak Magnetic Field," *ACS Photonics* **5**(10), 3956–3961 (2018).
10. G. Armelles, L. Bergamini, N. Zabala, M. U. González, F. García, R. Alvaro, J. Aizpurua, and A. Cebollada, "Broad band infrared modulation using spintronic-plasmonic metasurfaces," *Nanophotonics* **8**(10), 1847–1854 (2019).
11. G. Armelles and A. Cebollada, "Active photonic platforms for the mid-infrared to the THz regime using spintronic structures," *Nanophotonics* **9**(9), 2709–2729 (2020).
12. J. J. C. Jacquet and T. A. Valet, "A new magneto-optical effect discovered on magnetic multilayers: the magnetorefractive effect," *Mater. Res. Soc. Symp. Proc.* **384**, 477–490 (1995).
13. A. Granovsky, Y. P. Sukhorukov, E. Gan'shina, and A. Telegin, "Magnetorefractive effect in magnetoresistive materials," In: M. Inoue, M. Levy, and A. V. Baryshev, eds. *Magnetophotonics: From Theory to Applications*, *Magnetophotonics*. SpringerBerlin, Heidelberg, Germany, Springer Series in Materials Science 178, 107–133 (2013).
14. V. G. Kravets, D. Bozec, J. A. D. Matthew, S. M. Thompson, H. Menard, A. B. Horn, and A. F. Kravets, "Correlation between the magnetorefractive effect, giant magnetoresistance, and optical properties of Co-Ag granular magnetic films," *Phys. Rev. B* **65**(5), 054415 (2002).
15. R. T. Mennicke, D. Bozec, V. G. Kravets, M. Vopsaroiu, J. A. D. Matthew, and S. M. Thompson, "Modelling the magnetorefractive effect in giant magnetoresistive granular and layered materials," *J. Magn. Magn. Mater.* **303**(1), 92–110 (2006).
16. C. Huck, J. Vogt, M. Sendner, D. Hengstler, F. Neubrech, and A. Pucci, "Plasmonic Enhancement of Infrared Vibrational Signals: Nanoslits versus Nanorods," *ACS Photonics* **2**(10), 1489–1497 (2015).
17. F. Falcone, T. Lopetegui, M. A. G. Laso, J. D. Baena, J. Bonache, M. Beruete, R. Marqués, F. Martín, and M. Sorolla, "Babinet Principle Applied to the Design of Metasurfaces and Metamaterials," *Phys. Rev. Lett.* **93**(19), 197401 (2004).
18. T. Zentgraf, T. P. Meyrath, A. Seidel, S. Kaiser, H. Giessen, C. Rockstuhl, and F. Lederer, "Babinet's principle for optical frequency metamaterials and nanoantennas," *Phys. Rev. B* **76**(3), 033407 (2007).
19. H. U. Yang, R. L. Olmon, K. S. Deryckx, X. G. Xu, H. A. Bechtel, Y. Xu, B. A. Lail, and M. B. Raschke, "Accessing the optical magnetic near-field through Babinet's principle," *ACS Photonics* **1**(9), 894–899 (2014).
20. G. Armelles, B. Caballero, A. Cebollada, A. Garcia-Martín, and D. Meneses-Rodríguez, "Magnetic Field Modification of Optical Magnetic Dipoles," *Nano Lett.* **15**(3), 2045–2049 (2015).

21. Y. Park, J. Kim, Y.-G. Roh, and Q.-H. Park, "Optical slot antennas and their applications to photonic devices," *Nanophotonics* **7**(10), 1617–1636 (2018).
22. S. S. P. Parkin, R. F. C. Farrow, R. F. Marks, A. Cebollada, G. R. Harp, and R. J. Savoy, "Oscillations of interlayer exchange coupling and giant magnetoresistance in (111) oriented permalloy/Au multilayers," *Phys. Rev. Lett.* **72**(23), 3718–3721 (1994).
23. G. Armelles, A. Cebollada, and F. García, "Au dependence of the mid infrared optical and magnetorefractive properties of Ni<sub>81</sub>Fe<sub>19</sub>/Au GMR multilayers," *Opt. Mater. Express* **9**(2), 923–931 (2019).
24. M. Hentschel, T. Weiss, S. Bagheri, and H. Giessen, "Babinet to the Half: Coupling of Solid and Inverse Plasmonic Structures," *Nano Lett.* **13**(9), 4428–4433 (2013).
25. COMSOL Inc. COMSOL Multiphysics. URL <https://www.comsol.com>.
26. F. Neubrech, A. Pucci, T. W. Cornelius, S. Karim, A. García-Etxarri, and J. Aizpurua, "Resonant Plasmonic and Vibrational Coupling in a Tailored Nanoantenna for Infrared Detection," *Phys. Rev. Lett.* **101**(15), 157403 (2008).
27. R. Adato, A. A. Yanik, J. J. Amsden, D. L. Kaplan, F. G. Omenetto, M. K. Hong, S. Erramilli, and H. Altug, "Ultra-sensitive vibrational spectroscopy of protein monolayers with plasmonic nanoantenna arrays," *Proc. Natl. Acad. Sci. U. S. A.* **106**(46), 19227–19232 (2009).
28. R. Semenyshyn, M. Hentschel, C. Huck, J. Vogt, F. Weiher, H. Giessen, and F. Neubrech, "Resonant Plasmonic Nanoslits Enable in Vitro Observation of Single-Monolayer Collagen-Peptide Dynamics," *ACS Sens.* **4**(8), 1966–1972 (2019).
29. F. Neubrech, C. Huck, K. Weber, A. Pucci, and H. Giessen, "Surface-Enhanced Infrared Spectroscopy Using Resonant Nanoantennas," *Chem. Rev.* **117**(7), 5110–5145 (2017).
30. J. Vogt, C. Huck, F. Neubrech, A. Toma, D. Gerbert, and A. Pucci, "Impact of the Plasmonic Near- and Far-Field Resonance-Energy Shift on the Enhancement of Infrared Vibrational Signals," *Phys. Chem. Chem. Phys.* **17**(33), 21169–21175 (2015).
31. G. Armelles, A. Cebollada, F. García, and C. Pecharrromán, "Magnetic modulation of mid-infrared plasmons using Giant Magnetoresistance," *Opt. Express* **25**(16), 18784–18796 (2017).